Cobalt adatoms on graphene: Effects of anisotropies on the correlated electronic structure

R. Mozara,[1,*] M. Valentyuk,[1,2] I. Krivenko,[1,3] E. Şaşıoğlu,[4,5] J. Kolorenč,[6] and A. I. Lichtenstein[1,2]

[1]*I. Institute of Theoretical Physics, University of Hamburg, Jungiusstraße 9, 20355 Hamburg, Germany*

[2]*Department of Theoretical Physics and Applied Mathematics, Ural Federal University, 19 Mira Street, Yekaterinburg, 620002, Russia*

[3]*LSA Physics, Randall Lab, University of Michigan, 450 Church Street, Ann Arbor, Michigan 48109-1040, USA*

[4]*Peter Grünberg Institute and Institute for Advanced Simulation, Forschungszentrum Jülich and JARA, 52425 Jülich, Germany*

[5]*Institute of Physics, Martin Luther University Halle-Wittenberg, Von-Seckendorff-Platz 1, 06120 Halle (Saale), Germany*

[6]*Institute of Physics, The Czech Academy of Sciences, Na Slovance 2, 18221 Prague, Czech Republic*

(Received 17 November 2017; published 20 February 2018)

Impurities on surfaces experience a geometric symmetry breaking induced not only by the on-site crystal-field splitting and the orbital-dependent hybridization, but also by different screening of the Coulomb interaction in different directions. We present a many-body study of the Anderson impurity model representing a Co adatom on graphene, taking into account all anisotropies of the effective Coulomb interaction, which we obtained by the constrained random-phase approximation. The most pronounced differences are naturally displayed by the many-body self-energy projected onto the single-particle states. For the solution of the Anderson impurity model and analytical continuation of the Matsubara data, we employed new implementations of the continuous-time hybridization expansion quantum Monte Carlo and the stochastic optimization method, and we verified the results in parallel with the exact diagonalization method.

DOI: 10.1103/PhysRevB.97.085133

I. INTRODUCTION

Graphene is a remarkable condensed-matter system with various promising applications. Field-effect electronic devices based on graphene [1] as well as a whole wafer-scale integrated circuit built out of graphene components [2] have been demonstrated. The material itself displays an abundance of exotic properties, many of which have their origin in the peculiar feature of the low-energy electronic excitations: they resemble massless Dirac fermions [3].

Enhanced functionality of materials can be achieved by introducing inhomogeneities, of which impurities are one important kind. The first experimental realization of Co adatoms on graphene was described by Mattos [4], who extensively discussed the adsorption geometry as well as the Kondo effect. Since then, only a few further realizations of magnetic impurities on graphene were reported, with controversial conclusions about the existence of the Kondo effect in graphene [5,6].

Diverse theoretical studies have been performed aiming at characterization of the Kondo effect in pseudogap systems in general, and in graphene in particular, see Refs. [7–16] and references therein. The system of a Co atom adsorbed on a single layer of graphene can be accurately represented by the Anderson impurity model (AIM). Jacob *et al.* considered the Kondo effect of the Co/graphene system by performing one of the first realistic many-body studies utilizing this model in the framework combining the density-functional theory with the one-crossing approximation (DFT+OCA) [16]. Our *ab initio* calculation of the Coulomb matrix yields a weaker repulsion when compared to the Coulomb vertex employed by Jacob *et al.* Consequently, we were not able to see the Kondo effect since the charge fluctuations were not sufficiently suppressed.

For an impurity placed on a surface, the two-dimensional constraint leads to a geometric symmetry breaking, which additionally to the crystal-field splitting and the orbital-dependent hybridization, induces a pronounced anisotropy of the Coulomb interaction at the impurity [17]. Since electronic screening in the z direction is weaker, electrons in the Co $d_{3z^2-r^2}$ orbital feel a stronger Coulomb repulsion, whereas in the directions parallel to the graphene surface the screening is stronger. It is most efficient for the most hybridized orbitals of the E_1 symmetry. To take these effects into account, we employed the constrained random-phase approximation (cRPA) to calculate the effective (partially screened) Coulomb interaction matrix [18,19]. Since graphene exhibits a high mobility of its conduction electrons [20], its electronic polarizability is rather large, leading to a strong renormalization of the repulsion strength. The present paper aims at an exploration of the effects of geometric anisotropy in the effective Coulomb matrix while solving the corresponding Anderson impurity model by the continuous-time quantum Monte Carlo (CTQMC) method. The results are cross-checked with the exact diagonalization (ED) technique.

This paper is organized as follows. In Sec. II, we describe the DFT setup. In Sec. III A, we introduce the AIM and how its corresponding Hamiltonian is obtained from DFT by projection onto correlated orbitals. Section III B describes the CTQMC algorithm for the solution of the AIM, and how analytical continuation of the Matsubara data is performed using the stochastic optimization method. Section III C explains how we performed the ED method. Section III D explains how we performed the cRPA to obtain the Coulomb matrix, and Sec. III E the method to obtain the corresponding anisotropic

*rmozara@physnet.uni-hamburg.de

TABLE I. First line: occupations and crystal-field splittings from DFT after projection by the PLO method. The window of energy bands was taken such that the total occupation agrees with the one of Co supplied in the VASP pseudopotential package. Second line: ccupations as computed by Jacob *et al.* [16].

$n_{\rm tot}$	n_{xy}	n_{yz}	$n_{3z^2-r^2}$	n_{xz}	$n_{x^2-y^2}$	$\varepsilon_{\rm F}$	ε_{xy}	ε_{yz}	$\varepsilon_{3z^2-r^2}$	ε_{xz}	$\varepsilon_{x^2-y^2}$
8.2016	0.8093	0.7487	0.9859	0.7485	0.8084	−2.273	−0.720	−0.564	−0.711	−0.541	−0.714
7.02	0.6875	0.5950	0.945	0.5950	0.6875						

double counting. Sections IV A–IV C present and discuss the QMC results, and in Sec. IV D, we compare QMC with ED. We conclude the paper in Sec. V.

II. DENSITY-FUNCTIONAL THEORY

DFT simulations have been performed to find the equilibrium geometry of the system, and to extract kinetic-energy and Coulomb parameters for the Anderson impurity model. We considered a supercell with the Co adatom above the single-layered $3\times3\times1$ graphene sheet.

To determine the equilibrium position of the adatom, we explored two possible configurations over graphene: top and hollow. This part of the work was done in the framework of the VASP package with projector augmented wave (PAW) basis set [21]. The cut-off energy of the basis was chosen as 500 eV and the GGA(PW91) [22] approximation was used for the exchange-correlation energy $E_{\rm xc}$. The relaxation of the chosen structures was performed on a $12\times12\times1$ Γ-centered **k**-point mesh until forces were smaller than 0.01 eV/Å. The graphene layer was kept fixed and the Co adatom was free to relax in all directions. A vacuum separation of 15.0 Å was chosen.

The hollow position of the Co adatom was found to be energetically more favored in comparison to the adsorption site on the top of the carbon atom, which is in agreement with previous work [8]. Therefore we focused only on the hollow position and all further calculations in this paper refer to this absorption geometry. The structural relaxation yielded a distance of the Co impurity from the graphene sheet of about 1.5Å, which is in line with previous findings for the used functionals [8,23]. The filling of the Co d orbitals at this equilibrium distance $n_{\rm tot}=8.2$ was calculated with the aid of the PLO method by taking into account 18 bands around the Fermi level (see Ref. [27] and Sec. III A below). Table I presents occupations of individual d orbitals.

Quantum-chemical calculations performed by Rudenko *et al.* predicted the electronic configuration $3d^9 4s^0$ with $S=1/2$ for the cobalt atom placed at 1.5 Å above the graphene sheet [24], whereas the $3d^8 4s^1$ configuration, which corresponds to our DFT solution, was stable at larger distances. At yet larger distances, they found the state of the free atom ($3d^7 4s^2$) to be the lowest-energy solution. Virgus *et al.* also observed the transition from $3d^7 4s^2$ over $3d^8 4s^1$ to $3d^9 4s^0$ when the Co impurity approaches the surface [25]. They obtained an equilibrium distance of the Co impurity in case of a $3d^8 4s^1$ configuration, which is comparable to our setting. The x-ray absorption spectra measured experimentally by Eelbo *et al.* also indicate that the Co adatom is in the $3d^8 4s^1$ electronic configuration [26]. Jacob *et al.*, on the other hand, found the filling of the Co d orbitals to be 7.5 in their DFT calculations, and the subsequent treatment of the electronic correlations within OCA pushed the filling to a lower value near 7.0 [16]. The distance of Co from the graphene surface that they obtained is comparable to ours, and we consider their filling additionally to our $n_{\rm tot}=8.2$ in the many-body calculations below.

III. ANDERSON IMPURITY MODEL: SETUP AND SOLUTION

A. From first-principles DFT to a model Hamiltonian

The Co adatom on graphene resembles the case of a magnetic impurity coupled to a noninteracting bath for which the Anderson impurity model can be employed. To obtain *ab initio* parameters for this AIM, we projected the DFT band structure obtained in Sec. II onto Wannier orbitals localized at the Co adatom. To this end, we used the PLO method [27]. Labeling the Bloch states $|\mathbf{k},n\rangle$ by the momentum **k** and the band index n, with **k** being from the first Brillouin zone, and the Bloch transformed Wannier orbitals with quantum numbers $\alpha=(\mathbf{r},l,m)$ by $L_{\alpha\mathbf{k}}$ (**r** is the position of the impurity within the unit cell, and the Bloch transform is the Fourier transform over the Bravais lattice), the projectors are given by $\mathcal{P}_{\alpha n}(\mathbf{k})=\langle L_{\alpha\mathbf{k}}|\mathbf{k},n\rangle$. The local Green's function of the Co adatom is thereby obtained from the Bloch Green's function $G^{\rm B}_n(\mathbf{k},i\omega)=[i\omega-\varepsilon_n(\mathbf{k})]^{-1}$, with $\varepsilon_n(\mathbf{k})$ the band dispersion relative to the chemical potential, as

$$G_{\alpha\beta}(i\omega)=\sum_{\mathbf{k}n}\mathcal{P}_{\alpha n}(\mathbf{k})G^{\rm B}_n(\mathbf{k},i\omega)\mathcal{P}^{+}_{\beta n}(\mathbf{k})$$
$$=[i\omega-\varepsilon-\Delta(i\omega)]^{-1}_{\alpha\beta}, \quad (1)$$

with the on-site crystal-field matrix $\varepsilon_{\alpha\beta}$ and the hybridization function $\Delta_{\alpha\beta}(i\omega)$.

The multiorbital single-impurity Anderson model can be decomposed into three parts:

$$H=H_{\rm Co}+H_{\rm g}+H_{\rm hyb}. \quad (2)$$

The first part is the local Hamiltonian for the Co d states:

$$H_{\rm Co}=\sum_{\alpha\beta\sigma}\left(\varepsilon_{\alpha\beta}-\mu^{\rm DC}_{\alpha}\delta_{\alpha\beta}\right)c^{+}_{\alpha\sigma}c_{\beta\sigma}$$
$$+\frac{1}{2}\sum_{\alpha\beta\gamma\delta\sigma\sigma'}U_{\alpha\beta\gamma\delta}\,c^{+}_{\alpha\sigma}c^{+}_{\beta\sigma'}c_{\delta\sigma'}c_{\gamma\sigma}. \quad (3)$$

The first term is the crystal-field matrix, which is diagonal, i.e., $\varepsilon_{\alpha\beta}=\varepsilon_{\alpha}\delta_{\alpha\beta}$. The greek indices α, β, γ, δ label the orbitals, which transform according to the irreducible representations of the C_{6v} point group: $E_2=\{xy,x^2-y^2\}$, $E_1=\{xz,yz\}$, and $A_1=\{3z^2-r^2\}$. The spin degrees of freedom are denoted as σ, σ'. The second term in Eq. (3) is the effective on-site Coulomb interaction we obtained by the cRPA method

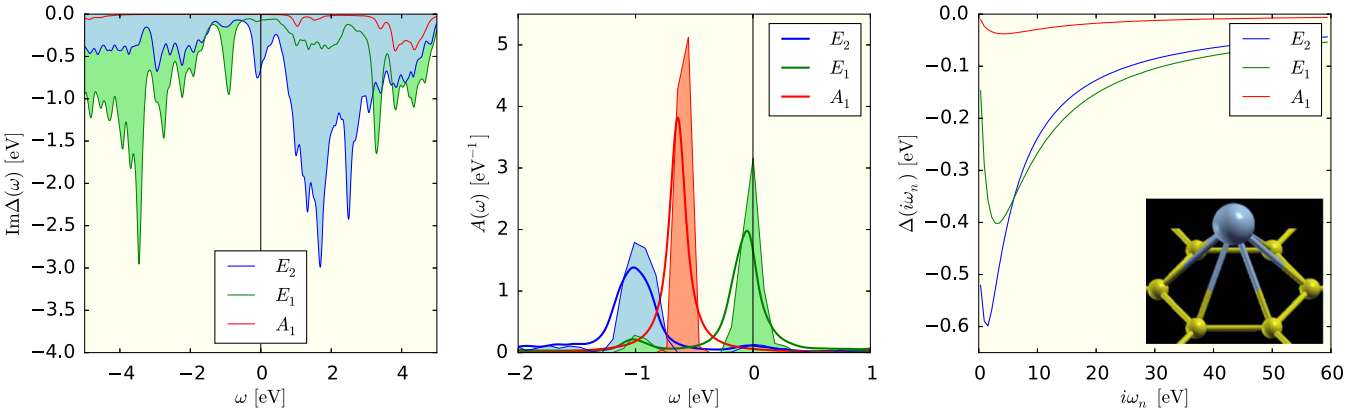

FIG. 1. (Left) Representation-resolved imaginary part of the real-frequency hybridization function $\Delta(\omega)$ for the d orbitals of the Co adatom obtained with the PLO method. (Middle) DFT (filled) and projected (unfilled) DOS $A(\omega)$. (Right) Matsubara hybridization function $\Delta(i\omega_n)$ at $\beta = 20\ \mathrm{eV}^{-1}$. Only the first 60 frequencies are displayed. The inset contains a picture of the geometry.

(Sec. III D). A double-counting (DC) correction μ_α^{DC} has to be subtracted to remove the Coulomb effects present in the DFT band structure.

The second part in Eq. (2) describes the spin-degenerate band structure of graphene,

$$H_{\mathrm{g}} = \sum_{\mathbf{k}n\sigma} \varepsilon_{\mathbf{k}n} f^{+}_{\mathbf{k}n\sigma} f_{\mathbf{k}n\sigma}\ , \tag{4}$$

where n is the band index. The on-site crystal-field matrix $\varepsilon_{\alpha\beta}$ and the energy bands $\varepsilon_{\mathbf{k}n}$ are measured with respect to the Fermi energy of graphene.

The last part in Eq. (2) is the hybridization between the adatom and graphene. It is given by

$$H_{\mathrm{hyb}} = \sum_{\mathbf{k}\alpha\sigma} (V_{\mathbf{k}\alpha} c^{+}_{\alpha\sigma} f_{\mathbf{k}\alpha\sigma} + \mathrm{H.c.}). \tag{5}$$

The electron hopping processes to and from the impurity preserve the local symmetry and hence the hopping amplitudes $V_{\mathbf{k}\alpha}$ are diagonal in the basis of the irreducible representations of the point group. The graphene states $f_{\mathbf{k}\alpha\sigma}$ are projections of $f_{\mathbf{k}n\sigma}$ onto this basis. The diagonal hybridization function characterizing the coupling between the adatom and graphene is obtained after integrating out the graphene degrees of freedom. It is defined as

$$\Delta_\alpha(i\omega) = \sum_{\mathbf{k}\alpha} \frac{|V_{\mathbf{k}\alpha}|^2}{i\omega - \varepsilon_{\mathbf{k}\alpha}}. \tag{6}$$

Real-energy and Matsubara representations of the hybridization function and the density of states for all five d orbitals are presented in Fig. 1. Features of the real-energy hybridization for the metallic impurity on graphene repeat findings of Wehling *et al.* [8]: one can see an almost complete suppression of the A_1 orbital whereas E_1 and E_2 form a symmetric slope around the Dirac point that is shifted slightly to the lower energy by an amount of $\mu = 0.2$ eV. This might be an effect of the supercell repetition with periodic occurrence of the Co adatom, effectively doping the graphene sheet, whereas a single adatom on an infinite sheet would not produce such a shift of the Fermi level. On the other hand, Mattos reported the same value for the chemical potential together with a low Kondo temperature [4] (being discussed in other references [8,10,28]).

B. Quantum Monte Carlo method and analytical continuation

The interacting impurity Green's function of the Anderson impurity model is given as

$$G_{\alpha\sigma}(i\omega) = \left[i\omega - \varepsilon_\alpha + \mu_\alpha^{\mathrm{DC}} - \Delta_\alpha(i\omega) - \Sigma_\alpha(i\omega)\right]^{-1}. \tag{7}$$

The electronic self-energy $\Sigma(i\omega)$ containing all Coulomb correlation effects was computed employing the hybridization-expansion variant of the continuous-time quantum Monte Carlo (CTHYB QMC) method. The CTHYB solver developed by the TRIQS collaboration [29,30] implements two important optimizations, namely a caching scheme based on a binary-tree data structure [31], and a novel scheme to automatically reduce the local Hamiltonian H_{Co} to a block-diagonal form (see Sec. 4 of Ref. [30] for details). These optimizations enable solving five-orbital impurity models with the rotationally invariant Coulomb matrix (referred to as Slater from now on) as well as with the cRPA approximation of the interaction matrix in a reasonable time. The "autopartition" algorithm gives a much finer block structure of the local Hamiltonian than one would get from the standard partitioning based on the occupation quantum numbers: $\hat{N}_\uparrow$ and $\hat{N}_\downarrow$ quantum numbers would result in $(2l+2)^2 = 36$ diagonal blocks, while we got 132 blocks in both Slater and cRPA cases (cubic harmonics have been used as the local orbital basis).

Typical computational time taken by one QMC simulation has varied from a few hundreds to a few thousands core hours. Actual values strongly depended on the local occupations as well as on the temperature.

The analytical continuation of the imaginary-time data has been performed using a recently established TRIQS-based implementation of Mishchenko's stochastic optimization method (SOM) [32]. This method amounts to a stochastic solution of the Fredholm integral equation of the first kind,

$$G_\alpha(\tau) = -\int_{-\infty}^{\infty} d\epsilon \frac{e^{-\tau\epsilon}}{1+e^{-\beta\epsilon}} A_\alpha(\epsilon). \tag{8}$$

For a given thermal Green's function $G_\alpha(\tau)$ measured in a QMC simulation (index α runs over all orbital and spin indices) a number of approximate particular solutions $A_\alpha(\epsilon)$ are constructed. Each particular solution is written as a superposition of N rectangles $\{c_i, w_i, h_i\}$ with the total spectral weight fixed to 1,

$$A_\alpha(\epsilon) = \sum_{i=1}^{N} h_i \theta(\epsilon - [c_i - w_i/2])\theta([c_i + w_i/2] - \epsilon),$$

$$1 = \sum_{i=1}^{N} h_i w_i.$$

A Markovian walk in the space of such superpositions is organized in order to find a minimum of the residue functional corresponding to the Fredholm equation (8). The Markov chain is started from a randomly generated configuration, typically 500–1000 times. Every time it results in another particular solution. Eventually, all particular solutions found by different Markov chains are averaged, so that stochastic noise is approximately canceled. For a more in-depth description of the algorithm we refer to the original paper of Mishchenko *et al.* [33].

C. Exact diagonalization

As an alternative method to QMC, we employ also the exact diagonalization, or more accurately, the Lanczos method. That way, the spectral functions of the impurity model are directly accessible without the need for analytical continuation but at the cost of discretized hybridization function. This discretization amounts to a replacement of the continuous spectrum $\varepsilon_{\mathbf{k}\alpha}$ with a discrete spectrum $\epsilon_{k\alpha}$ in Eqs. (4) and (5), where k takes values $1,2,\ldots,K$. The parameters $\epsilon_{k\alpha}$ and $V_{k\alpha}$ of such a finite impurity model are determined by minimization of a weighted sum of squares [34,35]

$$d_\alpha = \sum_{n>0} \frac{1}{\omega_n^r} \left| \Delta_\alpha(i\omega_n) - \sum_{k=1}^{K} \frac{V_{k\alpha}^2}{i\omega_n - \epsilon_{k\alpha}} \right|^2 \qquad (9)$$

for each of the Co d orbitals $\alpha = E_1$, E_2, and A_1. In the formula, Δ_α stands for the diagonal element of the DFT hybridization function, Eq. (1). The result of the fit for $\beta = 1/(k_B T) = 20$ eV^{-1}, $K = 4$, and $r = 1/2$ is shown in Fig. 2. The fits represent the DFT hybridization function very accurately, at least by visual inspection. For each α, there are two energies $\epsilon_{k\alpha}$ negative (that is, below the Fermi level) and two energies $\epsilon_{k\alpha}$ positive (above the Fermi level). Since the hybridization in the A_1 orbital is much smaller than in the E_1 and E_2 orbitals, it is neglected in all our ED calculations. For one particular setting of the Coulomb vertex, we have explicitly checked that dropping the A_1 hybridization, indeed, has a very small effect on the quantities of interest.

The fitted impurity model with four bath orbitals attached to each of the Co E_1 and E_2 orbitals is too large to be fully solved by the Lanczos method. To make the solution manageable, we employ a reduced many-body basis inspired by the work of Gunnarsson and Schönhammer [36,37]. A cutoff M is introduced for each N-electron Hilbert space $\mathcal{H}_N$, and the diagonalization is performed only in a subspace,

$$\mathcal{H}_N^{(M)} = \{|d^{N-N_b^<-n+m}\, b^n \underline{b}^m\rangle, \quad 0 \leqslant m+n \leqslant M\}. \qquad (10)$$

In this notation, $d^{N-N_b^<-n+m}$ indicates $N - N_b^< - n + m$ electrons in the Co d shell, b^n indicates n electrons in the bath orbitals above the Fermi level, and $\underline{b}^m$ means m holes in the bath orbitals below the Fermi level. The symbol $N_b^<$ denotes the number of bath orbitals located below the Fermi level ($N_b^< = 2 \times 10 = 20$ in the present case). This Hilbert-space reduction can be viewed as an expansion in the hybridization parameters $V_{k\alpha}$ around the atomic limit, that is, around the Hilbert space $\mathcal{H}_N^{(0)} = \{|d^{N-N_b^<}\, b^0\, \underline{b}^0\rangle\}$. We use the cutoff $M = 5$ and we have verified that this setting provides essentially converged spectral densities.

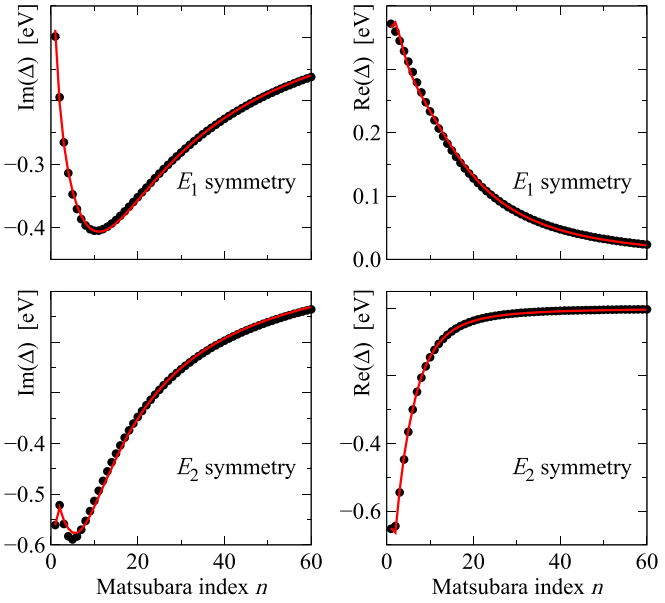

FIG. 2. Fit of the finite impurity model (lines) to the real and imaginary parts of the DFT hybridization function (dots) using Eq. (9). Only the first 60 Matsubara frequencies are plotted but the fit included the lowest 1024 frequencies.

D. Effective Coulomb matrix from the constrained random-phase approximation

The effective, partially screened Coulomb interaction matrix was obtained for the given geometry using the cRPA method [38,39]. The supercell was enlarged to achieve a distance of 28.35 Å between two adjacent graphene layers. We employed the SPEX code [40], a part of the Jülich full potential linearized augmented-plane-wave (FLEUR) code family [41]. The calculation of the effective interaction in cRPA is based on the separation of a chosen set of target bands and on a consequent consideration of all polarization processes between target and other (screening) bands. In our calculation, we used 19 bands near the Fermi level to project onto the local basis of the five d states of the Co adatom.

The constructed 625 elements of the cRPA Coulomb matrix are shown in Fig. 3. One can contrast this cRPA interaction matrix with the conventional Slater matrix defined by parameters F_0, F_2, F_4. These parameters have been estimated from the

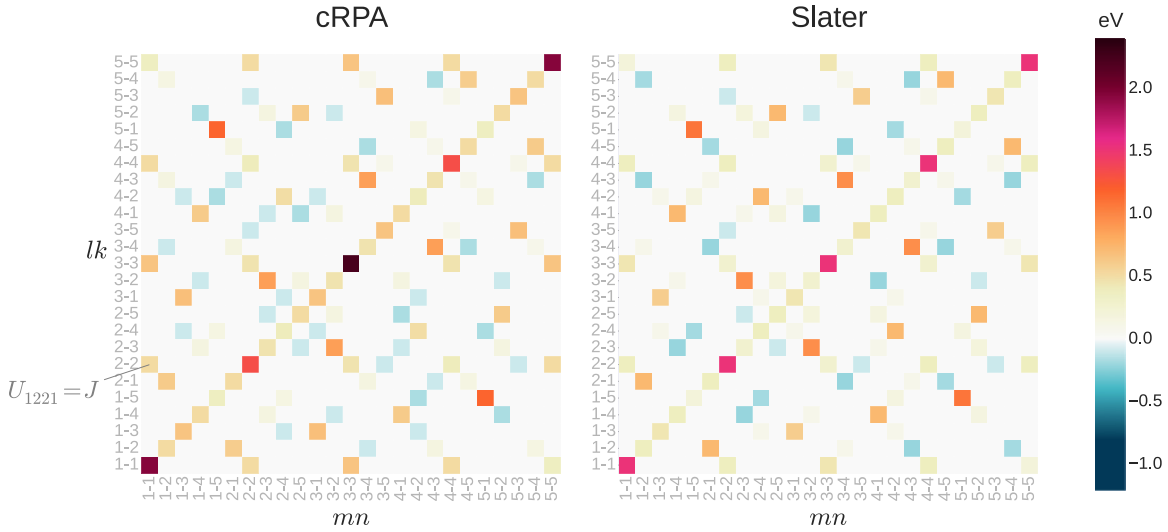

FIG. 3. Coulomb matrix for the d orbitals of the Co adatom obtained with the cRPA method (left) and subsequently rotationally averaged by the Slater approximation (right). The order of the orbitals is given by U_{mlkn}. The outlined element U_{1221} corresponds to the term $U_{1221}c^{+}_{1\uparrow}c^{+}_{2\downarrow}c_{2\downarrow}c_{1\uparrow}$, the index notation 1–5 runs for the orbital ordering (xy, yz, $3z^2 - r^2$, xz, $x^2 - y^2$).

cRPA Coulomb matrix via the effective repulsion and exchange parameters U, U', J as

$$U = \frac{1}{5}\sum_{m=1}^{5} U_{mmmm} = 1.76\ \text{eV},$$

$$U' = \frac{1}{20}\sum_{m\neq m'=1}^{5} U_{mm'mm'} = 0.73\ \text{eV},$$

$$J = \frac{1}{20}\sum_{m\neq m'=1}^{5} U_{mm'm'm} = 0.52\ \text{eV}, \tag{11}$$

$$F_0 = U/5 + 4U'/5 = 0.93\ \text{eV},$$

$$F_2 = 14J/1.625 = 4.44\ \text{eV},$$

$$F_4 = 0.625F_2 = 2.77\ \text{eV}. \tag{12}$$

First, the cRPA matrix displays a pronounced anisotropy in the density-density terms on the main diagonal of the plot. Interorbital exchange, which is responsible for suppressing parallel alignment on different orbitals, has been found to expose slightly higher amplitude for the cRPA matrix. Second, the intensity of the inter- and intraorbital spin-flip exchange terms (off-diagonal elements) appears to be lower in the cRPA case when compared to the spherically symmetric Slater vertex. Another visible feature is the change of the sign for interorbital spin-flip terms between cRPA and Slater matrices. The Coulomb matrix obtained by the cRPA method is rather small. It is reflected in the Slater parameters extracted from the symmetrized cRPA matrix, Eqs. (11) and (12).

The quantum-chemical considerations made by Rudenko *et al.* may provide a lower bound of the interaction strengths [24]. Our Slater parameters are by a factor of 2 smaller than theirs at comparable adatom-graphene distances. There are possibly three reasons why the cRPA Coulomb matrix turns out so small. First, the Co adatom is closer to the surface, that in turn increases overlaps with the graphene p orbitals, thus leading to an enhanced screening of the Coulomb interaction. Second, the finite distance between the layers of 28.35 Å, even though very large, might still artificially reduce the interaction matrix, as an extrapolation to the infinite layer distance has not been performed [23,42]. This effect, however, is not expected to contribute by more than 5% at our interlayer distance. And third, a systematic study revealed the screening of the Coulomb interaction at metal and insulator surfaces [43]. In contrast to common expectations, it is found that screening at metal surfaces is much more efficient than in bulk, and as a consequence the Hubbard U is reduced by 30%–40% compared to the bulk values. The situation in the case of the Co/graphene system is very similar where metallic screening is very efficient.

E. Anisotropic double counting

As the two-dimensional geometry of an impurity on a surface breaks rotational invariance, the Coulomb matrix exhibits an anisotropy between its components. The mean-field Coulomb terms incorporated in the DFT band structure have a corresponding anisotropy that has to be taken into account when the DC correction is introduced in Eq. (3). The exact expression for the DC correction is not known. We deduce it from the filling of the Co d orbitals found in DFT, since the DC correction acts similarly to the chemical potential and controls the filling of the impurity states in the impurity model. We considered two cases: the occupations resulting from our PLO projection procedure, and also the smaller occupations computed by Jacob *et al.* [16], all listed in Table I. The anisotropy requires the DC correction to be orbitally dependent, and for its determination we employed the Hubbard-I approximation, which takes into account a large portion of the electronic correlations. We started with the atomic Green's function augmented by the atomic Coulomb self-energy determined by exact diagonalization of H_{Co} with

TABLE II. DC correction (in units of eV) obtained for the anisotropic cRPA (middle columns) and the rotationally invariant Slater Coulomb matrix (last column). For comparison, the respective diagonal cRPA Coulomb matrix elements are (in units of eV) E_2: 1.95, E_1: 1.33, A_1: 2.23.

$n_{\mathrm{tot}}^{\mathrm{LDA}}$	$\mu_{\mathrm{E_2}}^{\mathrm{DC}}$	$\mu_{\mathrm{E_1}}^{\mathrm{DC}}$	$\mu_{\mathrm{A_1}}^{\mathrm{DC}}$	μ^{DC}
7.02	4.39	3.65	5.25	4.87
8.20	4.91	4.28	6.86	5.69

$\varepsilon_{\alpha\beta}$ set to zero,

$$G_\alpha^{\mathrm{at}}(i\omega) = \frac{1}{i\omega + \mu_\alpha^{\mathrm{DC}} - \Sigma_\alpha^{\mathrm{at}}(i\omega)}, \tag{13}$$

and then supplied the crystal-field splitting and the hybridization,

$$G_\alpha^{\mathrm{HIA}}(i\omega) = \frac{1}{i\omega - \varepsilon_\alpha + \mu_\alpha^{\mathrm{DC}} - \Sigma_\alpha^{\mathrm{at}}(i\omega) - \Delta_\alpha(i\omega)}. \tag{14}$$

We included the crystal-field splitting after calculating the atomic self-energy since its effect is small as compared to the Coulomb effects, and the thus obtained DC correction matches superiorly the DFT occupations in the subsequent full QMC simulation. Then, the minimization of the distance

$$\left\| n_{\mathrm{tot}}^{\mathrm{LDA}} - n_{\mathrm{tot}}^{\mathrm{HIA}} \right\|^2 = \sum_\alpha \left| n_\alpha^{\mathrm{LDA}} - n_\alpha^{\mathrm{HIA}} \right|^2 \tag{15}$$

is performed using the differential evolution procedure [44] as implemented in SCIPY. Differential evolution is a global optimization method, which is able to find the global minimum of a multivariate and possibly nondifferentiable function in relatively short time.

For the symmetrized Coulomb matrix in the Slater approximation, we calculated the DC correction in the around mean-field (AMF) limit given by the expression

$$\mu^{\mathrm{DC}} = n_{\mathrm{tot}}^{\mathrm{LDA}} \left[U\left(1 - \frac{1}{2N}\right) - J\left(\frac{1}{2} - \frac{1}{2N}\right) \right], \tag{16}$$

where $N = 2l + 1$ with $l = 2$. The choice of the AMF DC correction was motivated by its superior performance in the full QMC test simulations as compared to the fully localized limit (FLL).

The usual way to determine the isotropic DC correction is to identify the U in Eq. (16) with F_0 in Eq. (12) and J with the one in Eq. (11). For our calculations, we determined U and J by spherically averaging the Coulomb matrix twice, which yields U in Eq. (16) to be directly F_0 in Eq. (12), while the Hund's coupling is reduced to $J = 0.37$ eV. The results are summarized in Table II. The magnitude of the anisotropic DC corrections follows the Coulomb strength in the respective directions, as may also be compared with Fig. 3.

IV. DISCUSSION OF QMC RESULTS

QMC has been performed at $\beta = 20\ \mathrm{eV}^{-1}$, using 2.0×10^6 updates and 5.0×10^5 warmup updates on each core, and measuring at each 50th update. The set of possible updates contained double as well as global moves, the latter including global spin-flips and global orbital permutations of vertex

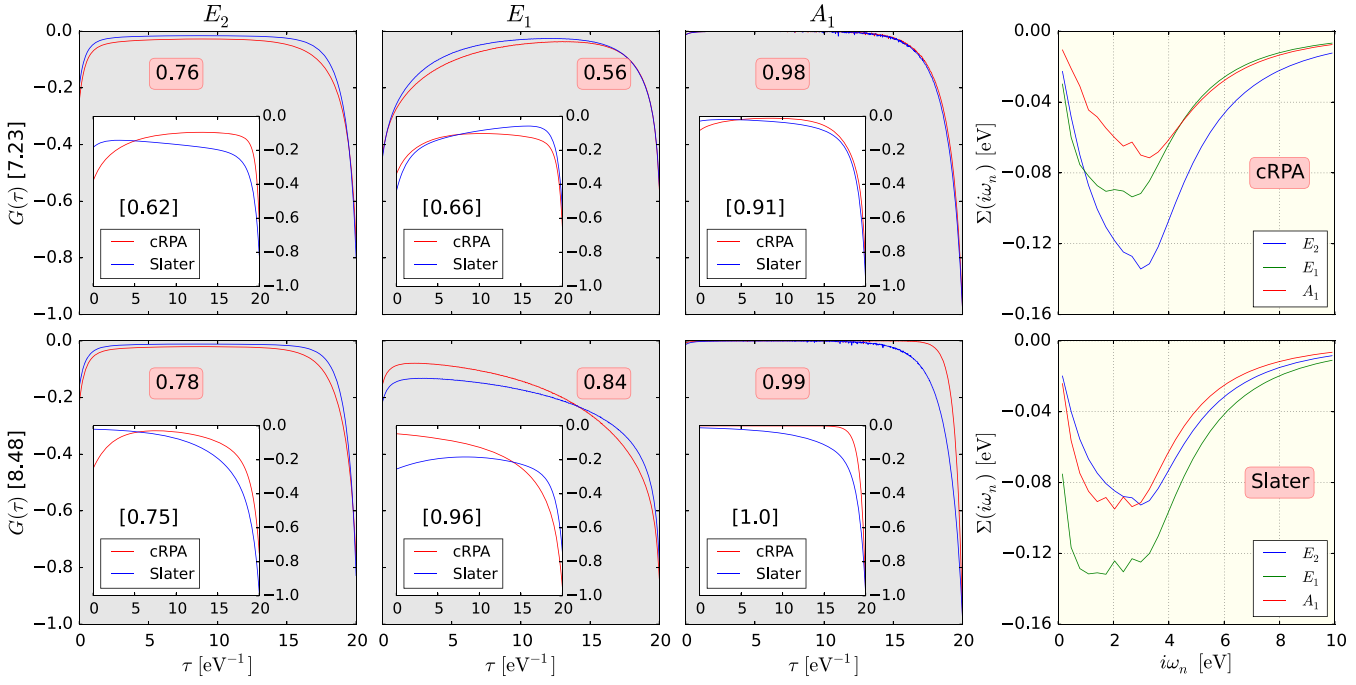

FIG. 4. (First three columns) Comparison between the representation-resolved imaginary-time Green's functions $G(\tau)$ for 5 d orbitals of the Co impurity calculated with the cRPA and the Slater Coulomb matrix. Total cRPA occupations are given in squared brackets, and orbital ones in round boxes. The upper and lower row contain the full QMC Green's functions at lower and higher filling, respectively, together with the atomic solution in the insets (orbital occupations in brackets). Calculations were performed at $\beta = 20\ \mathrm{eV}^{-1}$. (Last column) Representation-resolved Matsubara self-energy $\Sigma(i\omega_n)$ calculated with the cRPA (upper row) and the Slater Coulomb matrix (lower row), both at higher Co filling. Only the first 10 frequencies are displayed for a better resolution of the low-energy behavior.

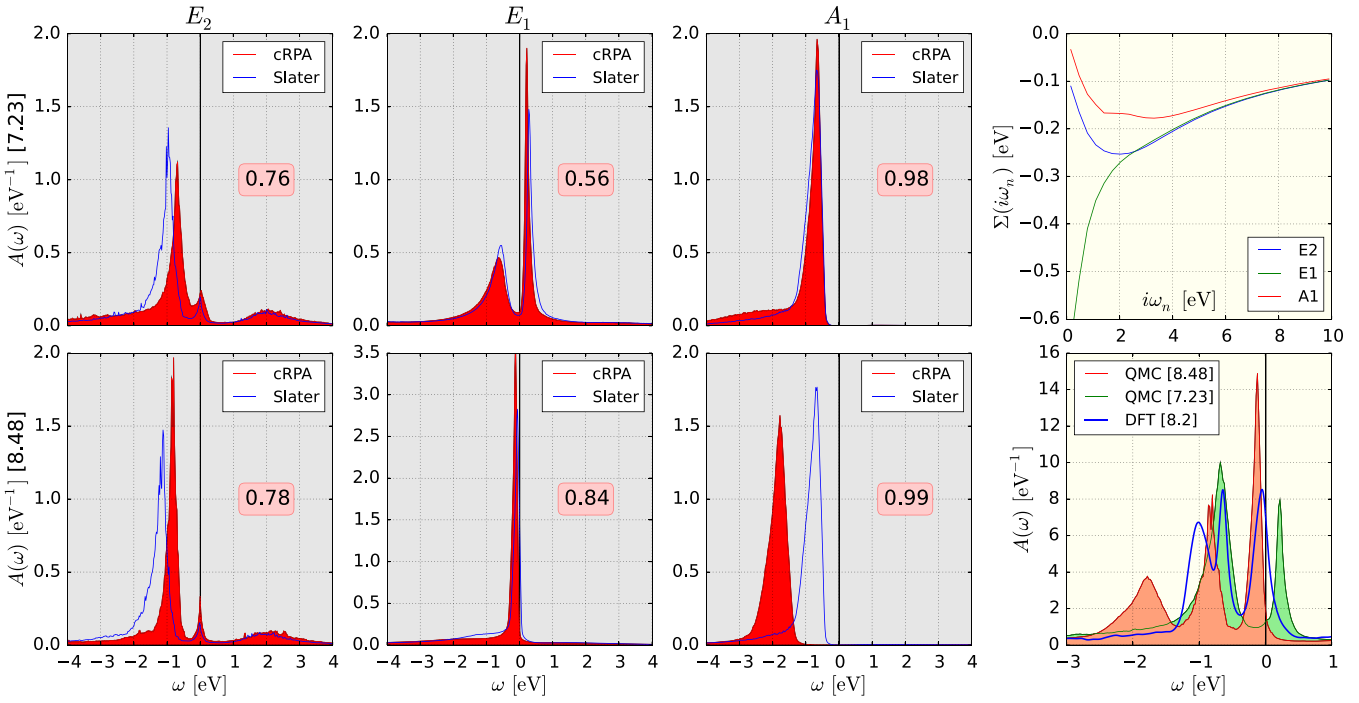

FIG. 5. (First three columns) Comparison between the representation-resolved DOS $A(\omega)$ for the d orbitals of the Co impurity calculated with the cRPA and the Slater Coulomb matrix. The upper and lower rows contain the DOSes at lower and higher Co filling, respectively. Total cRPA occupations are given in squared brackets, and orbital ones in round boxes. The spectra are obtained from the imaginary-time Green's functions in Fig. 4 by analytical continuation with the SOM solver. (Upper right) Representation-resolved Matsubara self-energy $\Sigma(i\omega_n)$ calculated with the cRPA Coulomb matrix at lower Co filling. Tail fitting was performed between the 10th and the 20th Matsubara frequency. (Lower right) Comparison between the QMC (with the cRPA Coulomb matrix) and the DFT total DOSes (total occupations in squared brackets).

indices. The calculations have been performed on 192 cores in parallel and took around 14–15 hours.

A. Physical importance of cRPA

The imaginary-time Green's functions obtained after solving the multiorbital AIM by the methods described in Sec. III B are displayed in Fig. 4. The results obtained with the full cRPA Coulomb matrix are compared to the ones with the Slater matrix. Rotationally averaging the Coulomb matrix by the Slater approximation slightly reduces the overall weight of the interaction strength, and some portions are redistributed, as it is seen in Fig. 3. The most pronounced differences occur for the higher filling considered, $n_{\mathrm{tot}} = 8.2$, especially in the A_1 representation. The hybridization in A_1 is small, thus the effect solely stems from the Coulomb interaction and its reduction in the spherical case. Lowering the Co filling by adjusting the DC correction presents the orbitals with E_1 symmetry as flexible with respect to their occupation, and E_1 crosses the Fermi level. This is a consequence of the orbitals within this representation being the most hybridized as well as having the strongest partial screening of the Coulomb interaction.

From the imaginary-time Green's function, we performed analytical continuation using SOM, and the results are summarized in Fig. 5. In agreement to the Green's functions, the differences for the lower filling are not as pronounced as for the higher one. Corresponding to the difference in the A_1 orbitals at higher Co filling, the peak is shifted towards lower values for the cRPA matrix. Considerable differences, though not qualitative in nature, can also be seen for the orbitals with E_2 symmetry where the main peak below the Fermi level is slightly shifted. The overall shape of all spectra remains the same, including the shape and position of subpeaks and shoulders. Thus considering anisotropies induced by the breaking of rotational invariance yields spectra that are largely invariant. One may thus conclude that the spectra obtained with the full cRPA Coulomb matrix coincide with the Slater approximation in many important aspects if the DC corrections are chosen such that the impurity filling coincides in both cases.

Notwithstanding the similar shapes of the spectra obtained with the cRPA and the Slater Coulomb matrix, the self-energies show considerable differences at low energies. As Co on graphene at higher Co filling of 8.2 is a usual Fermi-liquid, the self-energies should tend to zero at very low energies. This property is better resolved with the calculations using the cRPA matrix as one may observe in Fig. 4. There is also a change of the order of the self-energy strengths between the orbitals of E_1 and E_2 symmetry, and they intersect in the cRPA case. The interchange at very low energies between the one of E_2 and A_1 symmetry is in agreement with the interchange of the peaks in the corresponding spectra in Fig. 5. The relevance of taking into account anisotropies in the Coulomb matrix by the cRPA lies in the calculation of the self-energies. In particular, eventual estimation of Kondo parameters will rely on a proper determination of the self-energies. Further physical insights into the effects of anisotropy of the self-energy on the electronic configuration will be discussed in Sec. IV C.

TABLE III. Total and representation-resolved Co d-shell occupations, ground state energies $\varepsilon_{\mathrm{GS}}$, and expectation values of the local Hamiltonin $\langle H_{\mathrm{Co}}\rangle$ at $\beta = 20\,\mathrm{eV}^{-1}$. The upper part of the table corresponds to the full impurity model, the lower part to the local Hamiltonian H_{Co} alone not coupled to any bath.

	n_{tot}	n_{E_2}	n_{E_1}	n_{A_1}	$\varepsilon_{\mathrm{GS}}$[eV]	$\langle H_{\mathrm{Co}}\rangle$[eV]
Impurity problem						
cRPA vertex (QMC)	7.23	0.75	0.56	0.98	–	−22.30
	8.48	0.78	0.85	0.99	–	−29.09
cRPA vertex (ED)	7.26	0.76	0.55	1.00	−63.10	−22.32
	8.57	0.79	0.86	1.00	−69.66	−29.11
Slater vertex (QMC)	7.40	0.81	0.55	0.99	–	−25.09
	8.45	0.84	0.78	0.99	–	−31.18
Atomic problem						
cRPA vertex (ED)	6.94	0.62	0.66	0.91	−23.10	−23.07
	8.80	0.75	0.95	1.00	−29.71	−29.69
Slater vertex (ED)	7.43	0.81	0.56	0.97	−25.09	−25.05
	8.87	0.92	0.75	0.98	−31.74	−31.71

B. Electronic structure

Having a look at the occupations resulting from the QMC calculation with the cRPA Coulomb matrix in Table III, one observes the orbitals in the A_1 representation being nearly fully occupied, and the spectral weight is thus almost exclusively below the Fermi level as may be seen in Fig. 5. Furthermore, the calculations leave the occupation stable within the orbitals of E_2 symmetry, it is exactly 3.0 for the lower Co filling and 3.12 for the higher one. The additional electron at higher Co filling appears in the E_1 representation, as it may also be seen in the corresponding pDOS. The relevant single-particle peak changes its position from slightly above the Fermi level for lower Co filling to slightly below for higher filling, and it merges together with the other main spectral weight from below with a pronounced amplification of its height, while its width remains the same.

From the pDOS, it is seen that the E_2 representation has a small peak at the Fermi level. This peak can also be seen in the pDOS obtained in ED, see Fig. 6, and it corresponds to a bath state which happens to be very near the Fermi level. Furthermore, the self-energy in the E_1 representation shows a singularity upon approaching the low-energy region. This is due to the reduced filling of this representation and the re-emergence of the graphene pseudogap as an imprint on the pDOS of the Co impurity. At last, from the tDOS one observes that QMC with the cRPA Coulomb matrix yields the same overall electronic structure at higher filling like in case of the DFT-DOS projected on the impurity, that is, a three-peak structure, which is slightly stretched to higher energies due to the Coulomb effects. Note, however, the reordering of the peaks; in DFT, the lowest one belongs to E_2 while due to the large DC the lowest one in QMC is A_1. All these features together lead to the conclusion that, with the cRPA Coulomb matrix, QMC yields the electronic structure of the Co/graphene system very similar to DFT. In essence, this is a consequence of the strong screening predicted by cRPA.

C. Electronic configuration

The TRIQS CTHYB solver provides us with the reduced density matrix ρ_{Imp} of the Co adatom accumulated during the QMC simulation, and we are thus able to compute the grand canonical expectation value

$$\langle H_{\mathrm{Co}}\rangle = \mathrm{Tr}_{\mathrm{Co}}[\rho_{\mathrm{Imp}} H_{\mathrm{Co}}]. \tag{17}$$

The results are included in Table III.

We diagonalized the local Hamiltonian H_{Co} in Eq. (3), and obtained the ground state and excited states of the atomic problem containing the CF splitting. From Table III, one may see the atomic energy expectation values being near the ground-state energy of the local Hamiltonian. This means that the Boltzmann weights of the excited states are small, even at $\beta = 20\ \mathrm{eV}^{-1}$. As the QMC process describes the propagation of the local state from one eigenstate of the local Hamiltonian to another upon a hybridization event, physically relevant details of the impurity system are already reflected by the low-energy eigenstates. In particular, neglecting the small difference between the energy levels within one representation, the ground eigenstate of the local Hamiltonian corresponding to the higher filling has an SU(4) symmetry in the cRPA case, with one hole in the E_2 representation, while in the Slater case the hole is in the E_1 representation. In both cases, the ground state has nine electrons, and the orbital occupations change differently in taking into account the excited states, on the atomic as well as on the impurity level. Enforcing a lower impurity filling, the picture changes considerably: the cRPA case has ground eigenstate filling of seven with a spin-quartet being distributed over all orbitals, while in the Slater case it has a spin-triplet mostly in the E_1 representation with eight electrons in total. These different situations would definitely be reflected in eventual Kondo properties of the Co/graphene system, and apply to any system with pronounced geometric symmetry breaking where anisotropies in the Coulomb interaction occur. In contrast to this atomic picture, reflecting temperature-dependent features of the isolated impurity, the hybridization events lead to highly excited local states during the QMC process, thereby mixing the local states with bath states and leading to metallic behavior far away from the Kondo scenario. As our cRPA Coulomb matrix is small compared to the strength of the hybridization, this situation applies to our case. The local states are then dissolved into broad peaks as may be seen in the QMC DOS projected onto the single-particle states of the Co impurity, see Fig. 5.

To further characterize the effects of anisotropy on the electronic structure of the Co d orbitals, we computed the total and orbital-resolved charge and spin fluctuations $\Delta\mathcal{O} = \langle\mathcal{O}^2\rangle - \langle\mathcal{O}\rangle^2$, with $\mathcal{O}$ being the corresponding operator for the total or orbital occupancy or spin. The results are presented in Table IV together with the orbital-resolved effective masses given by

$$m^*_\alpha = 1 - \mathrm{Im}\,\Sigma'_\alpha(i\omega_n)\big|_{\omega_n=0} - \mathrm{Re}\,\Delta'_\alpha(0), \tag{18}$$

which are related to the inverse of the quasiparticle weights Z_α at the Fermi level. In both the cRPA and the Slater cases, the total charge fluctuation is on the order of one electron, and for both considered fillings the cRPA case exhibits stronger fluctuations than the Slater case. The effective mass anisotropy

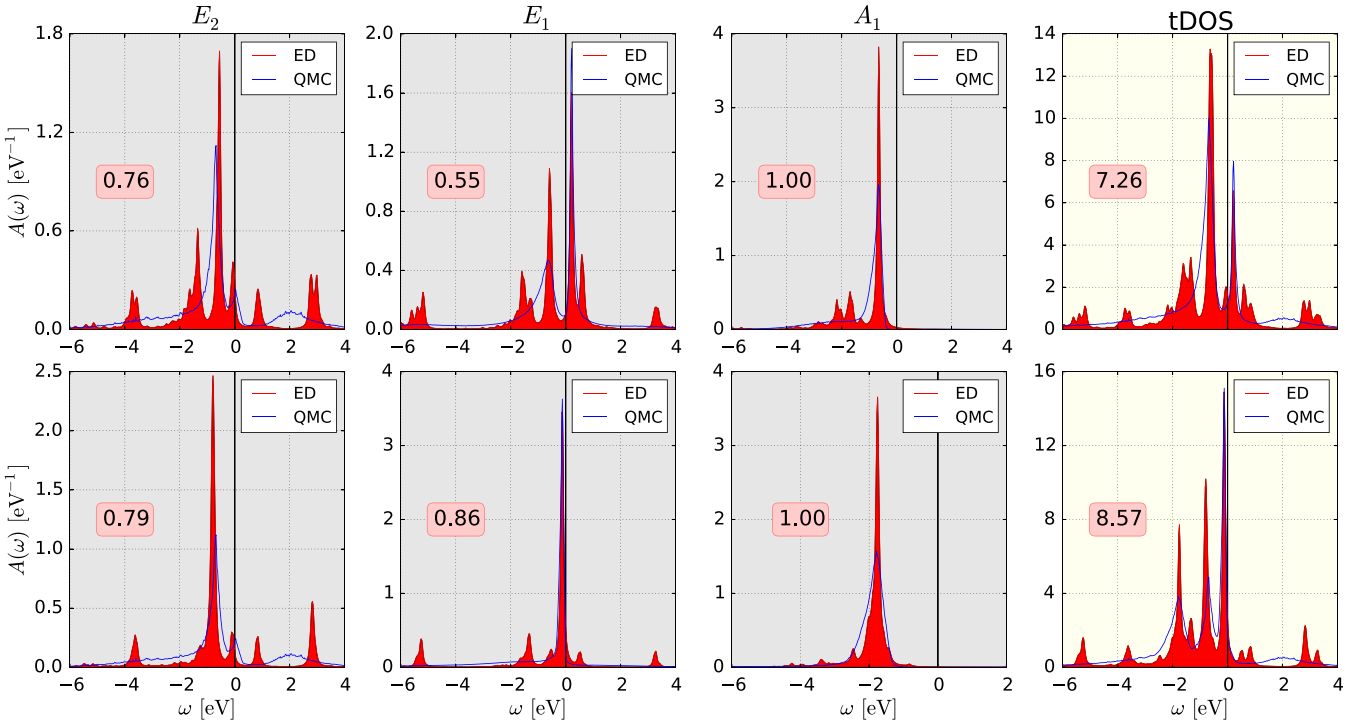

FIG. 6. (First three columns) Comparison between the representation-resolved DOS $A(\omega)$ for the d orbitals of the Co impurity calculated with QMC and ED using the cRPA Coulomb matrix. Orbital and total occupations obtained in ED are given in round boxes. The upper and lower rows contain the DOSes at smaller and larger fillings, respectively. The calculations were performed at $\beta = 20$ eV^{-1}. (Last column) Corresponding total DOSes $A(\omega)$ calculated at lower (upper row) and higher Co filling (lower row).

is solely due to the anisotropy of the self-energy. The hybridization term in Eq. (18) is essentially negligible. It can be clearly seen that changing the total impurity occupation away from the DFT value enhances the mass renormalization, especially in the orbitals of the E_1 symmetry where the non-Fermi-liquid behavior prohibits the use of Eq. (18) altogether. Generally, the effective mass scales with the Coulomb strength, and from Fig. 3, it is clear that the reduction in Coulomb strength in the E_2 orbitals upon the spherical average leads to a reduced effective mass. Although not pronounced, the reverse tendency applies to the orbitals of the E_1 symmetry.

D. Comparison of CTHYB with ED

The calculations employing the cRPA approximation to the Coulomb vertex were repeated with the finite-temperature exact-diagnolization method outlined in Sec. III C. The computed d-orbital occupations are listed in Table III. They are very close to the corresponding QMC results, the discrepancy in the total filling n_{tot} is smaller than 0.1 and the discrepancy in the orbital fillings is at most 0.02. The grand canonical expectation value of the local Hamiltonian is computed as

$$\langle H_{\text{Co}} \rangle = \frac{1}{Z} \sum_{\psi} e^{-\beta E_\psi} \langle \psi | H_{\text{Co}} | \psi \rangle \,, \tag{19}$$

where $|\psi\rangle$ and E_ψ are eigenfunctions and eigenvalues of the discretized impurity Hamiltonian, Eq. (2). This expression is equivalent to Eq. (17) and the data listed in Table III indeed confirm that.

The spectral densities calculated with CTHYB and ED are compared in Fig. 6. The agreement of the main features near the Fermi level is very good, discrepancies appear at higher energies where the analytical continuation of QMC data tends to overestimate broadening and ED shows artifacts of the bath discretization. The peak at the Fermi level in the E_2 spectrum appears to originate in a sharp feature of the bath density of states, Fig. 1, and not in any many-body Kondo physics.

TABLE IV. Total and representation-resolved orbital charge and spin fluctuations of the Co impurity displayed against its total d-shell occupation. The last three columns show the effective masses computed from the self-energy $\Sigma(i\omega_n)$.

vertex	n_{tot}	ΔN_{tot}	ΔN_{E_2}	ΔN_{E_1}	ΔN_{A_1}	ΔS^2_{tot}	ΔS^z_{tot}	$\Delta S^z_{E_2}$	$\Delta S^z_{E_1}$	$\Delta S^z_{A_1}$	$m^*_{E_2}$	$m^*_{E_1}$	$m^*_{A_1}$
cRPA	7.23	0.92	0.32	0.19	0.034	2.39	0.86	0.11	0.20	0.007	1.77	–	1.21
	8.48	0.97	0.31	0.24	0.015	1.09	0.37	0.09	0.07	0.003	1.21	1.20	1.07
Slater	7.40	0.83	0.29	0.18	0.026	1.95	0.76	0.08	0.20	0.006	1.38	–	1.15
	8.45	0.89	0.26	0.28	0.026	1.05	0.38	0.07	0.10	0.006	1.20	1.27	1.15

V. CONCLUSIONS

We performed a quantum many-body study of the Co/graphene system within the Anderson impurity model. DFT calculations have been performed to determine the ground-state properties and the basis for the projection onto localized orbitals centered at the Co impurity. To capture all geometric anisotropies in the Coulomb interaction, we calculated the effective, partially screened Coulomb matrix via cRPA. Having determined all the ingredients for the AIM, its QMC solution has been found by the TRIQS CTHYB solver, and subsequently analytically continued to the real axis by SOM. Within the QMC approach, effect of the cRPA Coulomb matrix has been compared against its approximate rotationally-invariant form. Additionally, we applied exact diagonalization to a subset of the investigated cases and we found a very good agreement between QMC and ED results. This comparison verifies the performance of the employed analytical continuation method, and in the same time it illustrates that ED can provide accurate results also in strongly hybridized cases far from the atomic limit.

As regards the differences between the cRPA and the Slater approximation, the electronic structure is not changed considerably, however, profound differences can be found in the single-particle self-energies of the correlated Co impurity. This is natural, as the self-energy contains most of the Coulomb correlation effects. The Coulomb interaction matrix obtained via cRPA is comparably small. Further considerations might thus be possible if it were determined to be larger; the differences between the cRPA and the Slater approximation are enhanced in this case, and the effects of anisotropies might thus compete against the hybridization dressing of the Co impurity, thereby revealing possible differences also in the electronic structure. Furthermore, an investigation of the possible existence and properties of the Kondo effect of Co on graphene incorporating all crystal-field effects and the graphene pseudogap could be pursued.

ACKNOWLEDGMENTS

We acknowledge financial support from the Deutsche Forschungsgemeinschaft (DFG) through Projects No. SFB668-A3 and No. DFG-LI 1413/8-1, from the Czech Science Foundation (GACR) under the Grant No. 15-05872J, and from the European Union's Horizon 2020 research and innovation program under Grant Agreement No. 696656 - GrapheneCore1. Access to computing facilities owned by parties and projects contributing to the National Grid Infrastructure MetaCentrum, provided under the program Cesnet LM2015042, is appreciated. The authors gratefully acknowledge the computing time granted by the John von Neumann Institute for Computing (NIC) and provided on the supercomputer JURECA at Jülich Supercomputing Centre (JSC) [45]. Computations were performed with resources provided by the North-German Supercomputing Alliance (HLRN).

[1] K. Novoselov, A. Geim, S. Morozov, D. Jiang, Y. Zhang, S. Dubonos, I. Grigorieva, and A. Firsov, Electric field effect in atomically thin carbon films, Science **306**, 666 (2004).

[2] Y.-M. Lin, A. Valdes-Garcia, S.-J. Han, D. Farmer, I. Meric, Y. Sun, Y. Wu, C. Dimitrakopoulos, A. Grill, P. Avouris, and K. Jenkins, Wafer-scale graphene integrated circuit, Science **332**, 1294 (2011).

[3] A. H. Castro Neto, F. Guinea, N. M. R. Peres, K. S. Novoselov, and A. K. Geim, The electronic properties of graphene, Rev. Mod. Phys. **81**, 109 (2009).

[4] L. S. Mattos, *Correlated Electrons Probed by Scanning Tunneling Microscopy*, PhD. thesis, Stanford University, 2009.

[5] V. W. Brar, R. Decker, H.-M. Solowan, Y. Wang, L. Maserati, K. T. Chan, H. Lee, Ç. O. Girit, A. Zettl, S. G. Louie, M. L. Cohen, and M. F. Crommie, Gate-controlled ionization and screening of cobalt adatoms on a graphene surface, Nat. Phys. **7**, 43 (2011).

[6] J. Jobst, F. Kisslinger, and H. B. Weber, Detection of the Kondo effect in the resistivity of graphene: Artifacts and strategies, Phys. Rev. B **88**, 155412 (2013).

[7] K. Sengupta and G. Baskaran, Tuning Kondo physics in graphene with gate voltage, Phys. Rev. B **77**, 045417 (2008).

[8] T. O. Wehling, A. V. Balatsky, M. I. Katsnelson, A. I. Lichtenstein, and A. Rosch, Orbitally controlled Kondo effect of Co adatoms on graphene, Phys. Rev. B **81**, 115427 (2010).

[9] A. Saffarzadeh and G. Kirczenow, Scanning tunneling spectroscopy and Dirac point resonances due to a single Co adatom on gated graphene, Phys. Rev. B **85**, 245429 (2012).

[10] L. Fritz and M. Vojta, The physics of Kondo impurities in graphene, Rep. Prog. Phys. **76**, 032501 (2013).

[11] M. Kharitonov and G. Kotliar, Kondo effect in monolayer and bilayer graphene: Physical realizations of the multichannel Kondo models, Phys. Rev. B **88**, 201103(R) (2013).

[12] L. Li, Y.-Y. Ni, Y. Zhong, T.-F. Fang, and H.-G. Luo, The Kondo effect of an adatom in graphene and its scanning tunneling spectroscopy, New J. Phys. **15**, 053018 (2013).

[13] D. Mastrogiuseppe, A. Wong, K. Ingersent, S. E. Ulloa, and N. Sandler, Kondo effect in graphene with Rashba spin-orbit coupling, Phys. Rev. B **90**, 035426 (2014).

[14] M. Vojta, R. Bulla, and P. Wölfle, Critical quasiparticles in single-impurity and lattice Kondo models, Eur. Phys. J. Spec. Top. **224**, 1127 (2015).

[15] A. Allerdt, A. E. Feiguin, and S. Das Sarma, Competition between Kondo effect and RKKY Physics in Graphene Magnetism, Phys. Rev. B **95**, 104402 (2017).

[16] D. Jacob and G. Kotliar, Orbital selective and tunable Kondo effect of magnetic adatoms on graphene: Correlated electronic structure calculations, Phys. Rev. B **82**, 085423 (2010).

[17] P. Hansmann, L. Vaugier, H. Jiang, and S. Biermann, What about U on surfaces? Extended Hubbard models for adatom systems from first principles, J. Phys. Condens. Matter **25**, 094005 (2013).

[18] F. Aryasetiawan, M. Imada, A. Georges, G. Kotliar, S. Biermann, and A. I. Lichtenstein, Frequency-dependent local interactions and low-energy effective models from electronic structure calculations, Phys. Rev. B **70**, 195104 (2004).

[19] E. Şaşıoğlu, C. Friedrich, and S. Blügel, Effective Coulomb interaction in transition metals from constrained random-phase approximation, Phys. Rev. B **83**, 121101(R) (2011).

[20] F. Schedin, A. K. Geim, S. V. Morozov, E. W. Hill, P. Blake, M. I. Katselson, and K. S. Novoselov, Detection of individual gas molecules adsorbed on graphene, Nat. Mater. **6**, 652 (2007).

[21] G. Kresse and D. Joubert, From ultrasoft pseudopotentials to the projector augmented-wave method, Phys. Rev. B **59**, 1758 (1999).

[22] J. P. Perdew, J. A. Chevary, S. H. Vosko, K. A. Jackson, M. R. Pederson, D. J. Singh, and C. Fiolhais, Atoms, molecules, solids, and surfaces: Applications of the generalized gradient approximation for exchange and correlation, Phys. Rev. B **46**, 6671 (1992).

[23] T. O. Wehling, E. Şaşıoğlu, C. Friedrich, A. I. Lichtenstein, M. I. Katsnelson, and S. Blügel, Strength of Effective Coulomb Interactions in Graphene and Graphite, Phys. Rev. Lett. **106**, 236805 (2011).

[24] A. N. Rudenko, F. J. Keil, M. I. Katsnelson, and A. I. Lichtenstein, Adsorption of cobalt on graphene: Electron correlation effects from a quantum chemical perspective, Phys. Rev. B **86**, 075422 (2012).

[25] Y. Virgus, W. Purwanto, H. Krakauer, and S. Zhang, Ab initio many-body study of cobalt adatoms adsorbed on graphene, Phys. Rev. B **86**, 241406(R) (2012).

[26] T. Eelbo, M. WaŚniowska, P. Thakur, M. Gyamfi, B. Sachs, T. O. Wehling, S. Forti, U. Starke, C. Tieg, A. I. Lichtenstein, and R. Wiesendanger, Adatoms and Clusters of 3*d* Transition Metals on Graphene: Electronic and Magnetic Configurations, Phys. Rev. Lett. **110**, 136804 (2013).

[27] M. Karolak, T. O. Wehling, F. Lechermann, and A. I. Lichtenstein, General DFT++ method implemented with projector augmented waves: Electronic structure of $SrVO_3$ and the Mott transition in $Ca_{2-x}Sr_xRuO_4$, J. Phys. Condens. Matter **23**, 085601 (2011).

[28] H. Kusunose and K. Miyake, Competition between Hund-Rule Coupling and Kondo Effect, J. Phys. Soc. Jpn. **66**, 1180 (1997).

[29] O. Parcollet, M. Ferrero, T. Ayral, H. Hafermann, I. Krivenko, L. Messio, and P. Seth, TRIQS: A Toolbox for Research on Interacting Quantum Systems, Comp. Phys. Comm. **196**, 398 (2015).

[30] P. Seth, I. Krivenko, M. Ferrero, and O. Parcollet, TRIQS/CTHYB: A Continuous-Time Quantum Monte Carlo Hybridization Expansion Solver for Quantum Impurity Problems, Comp. Phys. Comm. **200**, 274 (2016).

[31] E. Gull, *Continuous-Time Quantum Monte Carlo Algorithms for Fermions*, PhD. thesis, ETH Zurich, 2008.

[32] I. Krivenko, *TRIQS-based Stochastic Optimization Method for Analytic Continuation*, https://github.com/krivenko/som.

[33] A. S. Mishchenko, N. V. Prokof'ev, A. Sakamoto, and B. V. Svistunov, Diagrammatic quantum Monte Carlo study of the Fröhlich polaron, Phys. Rev. B **62**, 6317 (2000)

[34] M. Caffarel and W. Krauth, Exact Diagonalization Approach to Correlated Fermions in Infinite Dimensions: Mott Transition and Superconductivity, Phys. Rev. Lett. **72**, 1545 (1994).

[35] A. Liebsch and H. Ishida, Temperature and bath size in exact diagonalization dynamical mean field theory, J. Phys. Condens. Matter **24**, 053201 (2012).

[36] O. Gunnarsson and K. Schönhammer, Electron spectroscopies for Ce compounds in the impurity model, Phys. Rev. B **28**, 4315 (1983).

[37] J. Kolorenč, A. B. Shick, and A. I. Lichtenstein, Electronic structure and core-level spectra of light actinide dioxides in the dynamical mean-field theory, Phys. Rev. B **92**, 085125 (2015).

[38] T. Miyake and F. Aryasetiawan, Screened Coulomb interaction in the maximally localized Wannier basis, Phys. Rev. B **77**, 085122 (2008).

[39] F. Aryasetiawan, K. Karlsson, O. Jepsen, and U. Schönberger, Calculations of Hubbard U from first-principles, Phys. Rev. B **74**, 125106 (2006).

[40] C. Friedrich, S. Blügel, and A. Schindlmayr, Efficient implementation of the GW approximation within the all-electron FLAPW method, Phys. Rev. B **81**, 125102 (2010).

[41] http://www.flapw.de.

[42] M. Rösner, E. Şaşıoğlu, C. Friedrich, S. Blügel, and T. O. Wehling, Wannier function approach to realistic Coulomb interactions in layered materials and heterostructures, Phys. Rev. B **92**, 085102 (2015).

[43] E. Şaşıoğlu, C. Friedrich, and S. Blügel, Strength of the Effective Coulomb Interaction at Metal and Insulator Surfaces, Phys. Rev. Lett. **109**, 146401 (2012).

[44] R. Storn and K. Price, Differential Evolution - A Simple and Efficient Heuristic for global Optimization over Continuous Spaces, J. Global Optim. **11**, 341 (1997).

[45] Jülich Supercomputing Centre, JURECA: General-purpose supercomputer at Jülich Supercomputing Centre, Journal of large-scale research facilities, **2**, A62 (2016).